Tracking Debris Cloud Fragments: An experimental method for measuring hypervelocity fragmentation in the context of validating numerical simulations

Erkai Watson [1*], Nathanael Durr [1], Martin Schimmerohn [1]

[1] Fraunhofer Institute for High-Speed Dynamics, Ernst Mach-Institut, EMI, 79104 Freiburg, Germany
[*] erkai.watson@emi.fraunhofer.de

ABSTRACT

We present the development of an experimental measurement technique designed for measuring hypervelocity impact fragmentation in the laboratory. The setup uses multiple high-speed cameras to record the debris fragments. The main steps of the algorithm are: fragment identification and tracking in each view, matching the fragments found in different views, and reconstructing the 3D trajectories of each fragment. The result is a method able to measure the 3D positions, 3D velocities, and sizes of individual debris cloud fragments to a level of detail unmatched by other experimental methods. We present an outlook of how the experimental hypervelocity fragmentation data collected is being used to validate state-of-the-art numerical simulations to better predict the fragmentation patterns and satellite breakup effects.

1 INTRODUCTION

The increasing number of objects orbiting in Earth's orbits constitute a growing risk to satellites operating in low earth orbit. Improving our understanding of the space debris environment is one step necessary for mitigating this risk and slowing its growth. Ground based sensors, such as radar and telescopes, are able to provide valuable information about the current debris environment, but are limited in their resolution. Small sub-centimeter pieces of debris are difficult, if not impossible to detect from ground-based sensors, yet they are still capable of damaging or disabling satellites due to their high incident velocities. Numerical simulations based on physical-mathematical models are one solution to better understanding the presence and effect of these smaller debris fragments in the orbital environment. While numerical simulations are a powerful tool for investigating and understanding hypervelocity impact (HVI) phenomena, their results are only relevant if the models can be shown to faithfully reproduce the physical reality of impact and fragmentation. To this end, high quality experimental data is needed to calibrate and validate numerical simulations.

Typical experimental measurements of HVI in the laboratory are only able to provide generalized or qualitative data on the fragmentation resulting from the impact. Such measurements are often made with high-speed cameras or radiographs and can measure the expansion velocities of prominent features of the debris cloud or provide experimental images for qualitative comparisons with numerical simulations. What is lacking, for the purpose of numerical validation, is more quantitative and statistical data on the properties of the individual debris cloud fragments.

A number of researchers have developed methods for tracking and measuring individual fragment properties from HVI. The earliest attempts focused on geological materials and used a laser sheet to selectively illuminate a small subset of particles at a time [1]. More complex analysis algorithms, such as Particle Image Velocimetry [2] and Particle Tracking Velocimetry [3] from fluid applications, allowed detailed data to be measured about material ejection from HVI in sand [4], [5].

The fragment tracking method described in this paper also traces its roots to the 2D tracking of ejecta in geological material using a laser sheet [6], [7]. The same method was applied to track HVI fragments of aluminum bumper plates in 2D [8]. Upgrading the fragment tracking method from 2D to 3D required new analysis algorithms [9] and additional cameras or mirror systems [10].

In this paper, we build upon previous developments and describe an experimental method which uses at least two high-speed cameras and is capable of measuring individual fragment positions and velocities in 3D. Additionally, fragment sizes can be estimated from the images allowing fragment kinetic energy and momentum to be directly measured. The uniquely detailed data that can be measured with this approach is being used to validate numerical simulations to a much higher level of detail than previously possible.

2 EXPERIMANTAL SETUP

Our fragment tracking method has relatively low setup requirements. All that is needed is two or more synchronized high-speed cameras and an adequate light source. Fig. 1 shows an example of an experimental setup at one of Fraunhofer EMI's light-gas gun facilities. In this setup, three high-speed cameras capable of micro- to nanosecond exposure times and framerates of up to 10 million frames per second, are placed in a closely packed

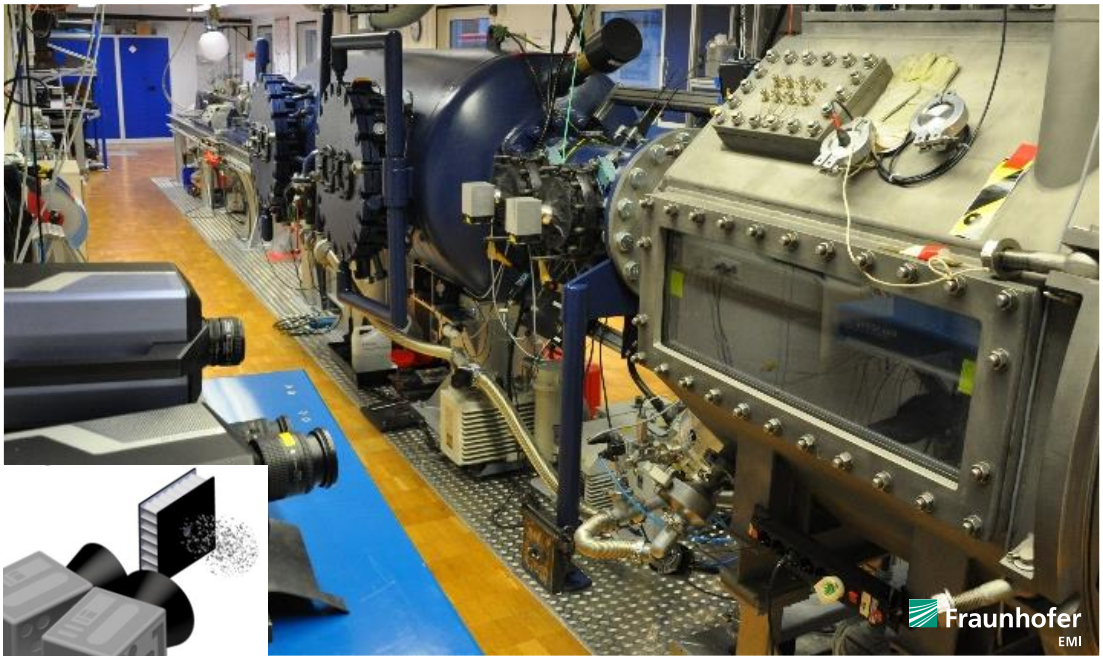

Figure 1. One of Fraunhofer EMI's light-gas gun facility showing the setup of three high-speed cameras. Bottom left insert: Schematic view of relative positions of camera, target, and debris fragments.

configuration to record the fragments generated upon HVI. A schematic view showing the relative positions of the cameras, the target, and the fragment cloud is shown in the lower left corner of Fig. 1. Illumination in this case is provided from behind the fragment cloud in a back-lit configuration using halogen flash lamps. This leads to shadowgraph recordings of the debris fragments. Front-lit experimental setups have also been successfully applied to our fragment tracking method.

For accurate 3D measurements, it is critical that the high-speed cameras be accurately synchronized to ensure each image sequence matches those of the other cameras. Alternatively, a single high-speed camera, with its image split into two separate views can also be used to avoid synchronization issues, as is described in [10].

The only other requirement for the experimental setup, is that the camera parameters, intrinsic and extrinsic, be known. This is typically measured with a camera calibration routine performed either directly before or directly after the experiment. For calibrating the cameras, we record dozens of images of a 2D checkerboard pattern of know dimension and calculate the cameras' intrinsic and extrinsic parameters based on Zhang's calibration method [11]. Radial and tangential distortion are corrected for with Brown's distortion model [12].

In this paper, we use a single experiment to illustrate the steps and results of the fragment tracking approach and the type of experimental data that can be reliable measured from each experiment. As our illustrative example, we use an impact experiment involving an aluminium sphere impact on a carbon fibre reinforced polymer (CFRP) honeycomb sandwich panel. The honeycomb sandwich panel used is typical of those found in modern satellites and consists of two 1 mm thick CFRP face sheet with 0°/45°/90° fibre orientations, and an aluminium honeycomb core for a total thickness of 32.5 mm. Fig. 2 shows a post-impact image of the sandwich panel.

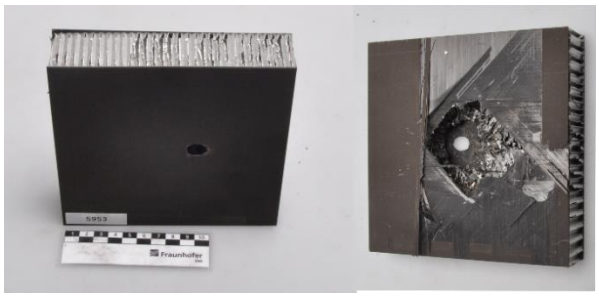

Figure 2. CFRP honeycomb sandwich panel after an impact with a 5.5 mm aluminium sphere at 7.0 km/s.

The impactor is a 5.5 mm aluminium sphere and is accelerated to 7.0 km/s. The impact angle is 45° to the target normal. The target chamber is evacuated to 8.25 mbar and is at room temperature.

The three cameras shown in Fig. 1 record the impact event at 66 666 frames per second, each with a field of view of approximately 40 x 25 cm. Fig. 3 shows a series of snapshots from the high-speed video from camera 1. In these images, the target is just outside the camera's field of view on the left side of each image. The impact direction is from left to right, and the ejected fragments also travel in this direction. The low frame rate, relative

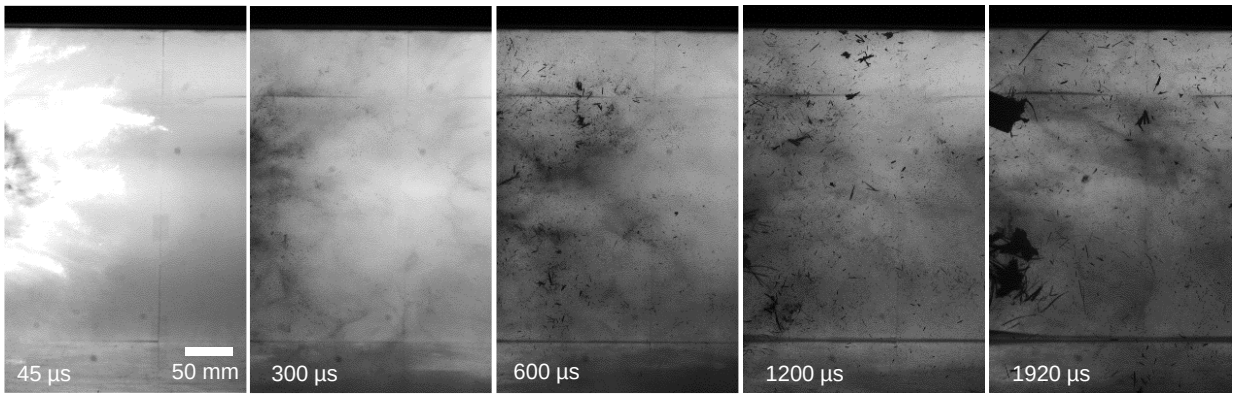

Figure 3. Image sequence from one high-speed video camera. Impact from left to right with target panel out of view to the left of each image.

to the impact velocity, was chosen in order to focus on the late-time fragments released from the CFRP face-sheets and aluminium honeycomb core, rather than the very fast and finely fragmented particles of the aluminium impactor. From the image sequence in Fig. 3, we see that fragment sizes begin small and gradually become larger, culminating in entire sections of the face sheet delaminating. Fragment shapes can also be qualitatively seen to start small and round and then progress to long thin fibre shapes.

It is our goal to track and measure as many of these fragments as possible, in order to determine their individual 3D velocities and sizes.

3 ALGORITHM & ANALYSIS

The algorithm used to perform fragment tracking can be broken into four major steps: detection, tracking, matching, and triangulation. This is shown schematically in Fig. 4. The first two steps, detection and tracking, are performed independently for each camera. Camera data is merged in the matching step. Finally, 3D quantities are reconstructed in the triangulation step.

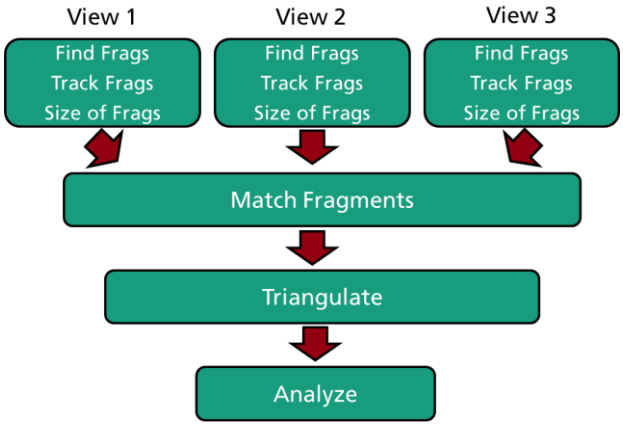

Figure 4. Workflow of the fragment tracking algorithm.

3.1 Fragment Detection and Tracking

The first step in any tracking algorithm is to detect the fragments. We do this independently for each image of a video sequence using standard image processing techniques including background subtraction, local mean subtraction, and thresholding. Fragments below a certain size threshold, usually one or two pixels, and above a certain threshold are removed.

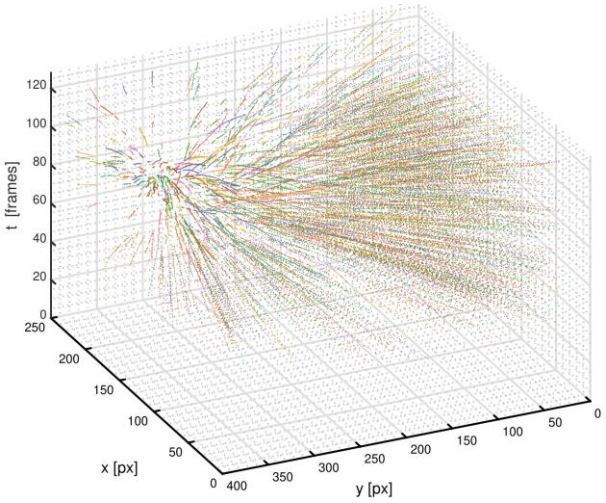

Figure 5. Tracked fragments in XYT space (2D + time).

Next, the detected points need to be tracked, or linked together into trajectories, along the length of the video. We achieve this by implementing a random sample consensus (RANSAC) [13] based algorithm specifically tailored to the constraints and characteristics of the HVI fragments. Most notable of these is the fact that after impact fragment travel in free-flight, with only negligible external forces acting to change a fragment's trajectory or velocity. Recognizing these unique characteristics allows us to accurately track fragment, even at very high particle per pixel densities, leading to robust results. Fig.

5 shows the results of fragment detection and tracking. Identified and tracked fragments are plotted in an XYT (2D + time) space. Fragments that represent the same object over time are shown in the same colour.

3.2 Fragment Size

Fragment sizes can be measured independently in each camera by segmenting the fragment foreground from the background. As shown in Fig. 6, a region of interest is defined about each fragment and the central fragment is identified and measured with the appropriate threshold. Since each fragment has already been tracked, the area of the same fragment can be measured over many frames.

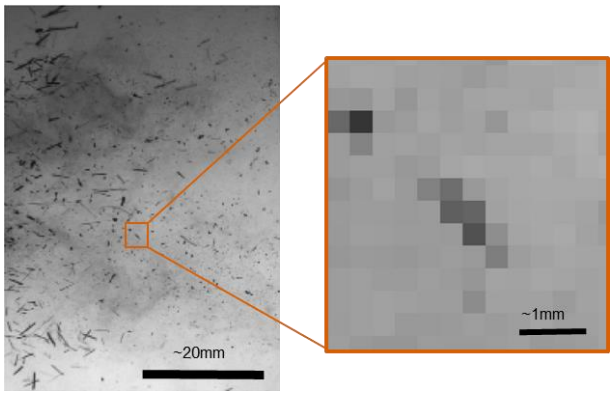

Figure 6. Fragment areas are measured by segmenting the foreground from the background.

An example of this is shown in Fig. 7, where a CFRP fragment is tracked. Fig. 7 shows a collage of images of the same fragment at consecutive time frames starting at the upper left corner and proceeding to the right. The CFRP fragment can be seen rotating over time. Despite the low resolution and noisy image background, the ability to make size measurements repeatedly, over the course of a fragment's trajectory considerably increases the reliability of the size measurement. The areas of the fragments in Fig. 7 are plotted over time in Fig. 8. Here the noisy nature of individual measurements is apparent as well as the advantages of having multiple measurements.

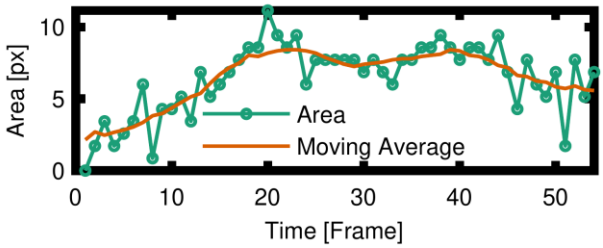

Figure 8. Fragment area measurements are averaged over time

3.3 Fragment Matching

The most challenging step in our fragment tracking algorithm is the matching step, also known as image correspondence in the photogrammetry and computer vision communities. The goal here is to match the same fragment, seen in different views, together. This task is challenging because it can only be done based on the position of the fragments. Additional information such as features, shape, or colour are not reliable enough to be used because of the small fragment sizes and low camera resolutions.

Fragment matching is made possible by using epipolar constraints as defined by the fundamental matrix between two cameras. The epipolar geometry of a camera pair is described by

$$\mathbf{l}'_1 = \mathrm{F}_{12}\mathbf{x}_1 , \qquad (1)$$

where F_{12} is the 3 x 3 fundamental matrix, $\mathbf{x}_1$ is 2D image coordinate in image 1, and $\mathbf{l}'_1$ is a line in image 2 on which the matching point must lie. The first two images of Fig. 9 schematically illustrate this two image scenario. Point $\mathbf{x}_1$ is identified in image 1 (top left) and the corresponding epipolar line $\mathbf{l}'_1$ is shown in image 2 (top right) as an orange line. Potential matches in image 2, $\mathbf{x'}_A$, $\mathbf{x'}_B$, and $\mathbf{x'}_C$ are shown in green. All three of these points are within the error tolerance of the epipolar line and could be potential matches. They therefore represent ambiguities that cannot be resolved without additional information.

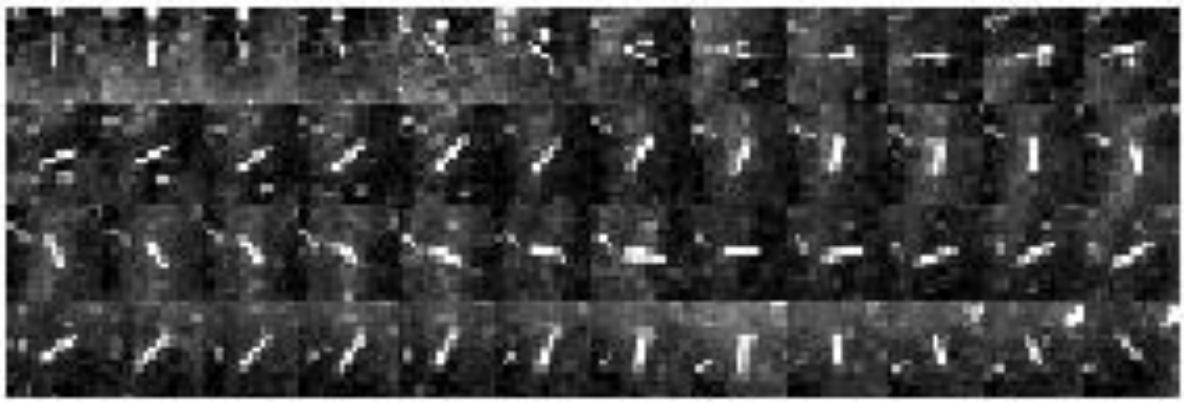

Figure 7. Zoomed in view of a single fragment over multiple time frames. The rotation of the fragment is visible.

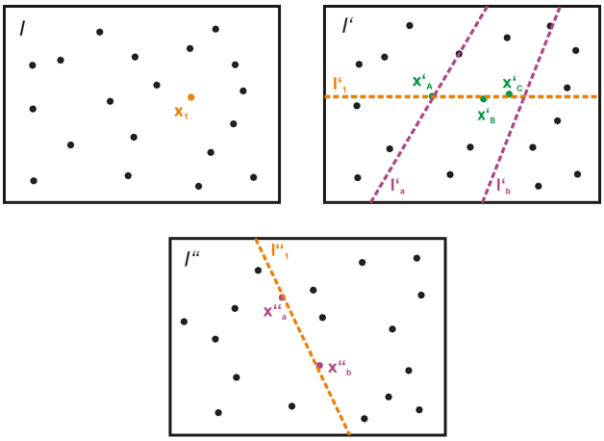

Figure 9. Epipolar geometry is used to match fragments between cameras.

To resolve such ambiguities, a third camera, shown in the bottom image of Fig. 9, can be used. Eq. 1 can again be used for points identified in image 3 to help resolve ambiguities in image 2. This is graphically shown with the intersection of the purple and orange epipolar lines in Fig. 9.

If three views are available, a much more elegant and robust solution is available via the three-view analogue of the two-view fundamental matrix, the trifocal tensor. Using the trifocal tensor, once a point has been matched in two views, it can be uniquely transferred to the third image with

$$x''^k = x^i l'_j T_i^{jk}, \tag{2}$$

using Einstein summation notation and where T is the trifocal tensor, x are image points, and l is an epipolar line. The prime and double prime indicate image two and three respectively.

3.4 Fragment Triangulation

Once tracked fragments have been matched to one another in all three views, the 3D positions of each matched fragment can be reconstructed via triangulation. The final step after triangulation is a bundle adjustment step to refine the final reconstructed positions.

4 RESULTS

In this section we present some of the measurement results that can be made with the fragment tracking method described in the last section. We continue with the same example experiment presented in Sec. 2.

Fig. 10 shows the last three experimental images from Fig. 3, this time with the completely tracked and matched fragments indicated with a small green dot and each velocity with an orange arrow. The velocities in this plot are 2D in-plane velocities. Due to the requirement that each fragment be uniquely matched in all three cameras, many fragments that are visible in Fig. 10 and have been tracked in this camera are not marked because a suitable match was not found in all three cameras. Large fragments, such as those seen in the last frame of Fig. 10, are also excluded from the tracking.

In Fig. 11 these same fragments, combined with those in cameras 2 and 3 are triangulated to show their 3D positions and 3D velocities. In the plots of Fig. 11, the bold red arrow represents the impact direction and the red dot the impact location on the CFRP panel. The CFRP panel is placed at a 45° angle to the impact axis such that its normal vector lies in the y-z plane. The coordinate

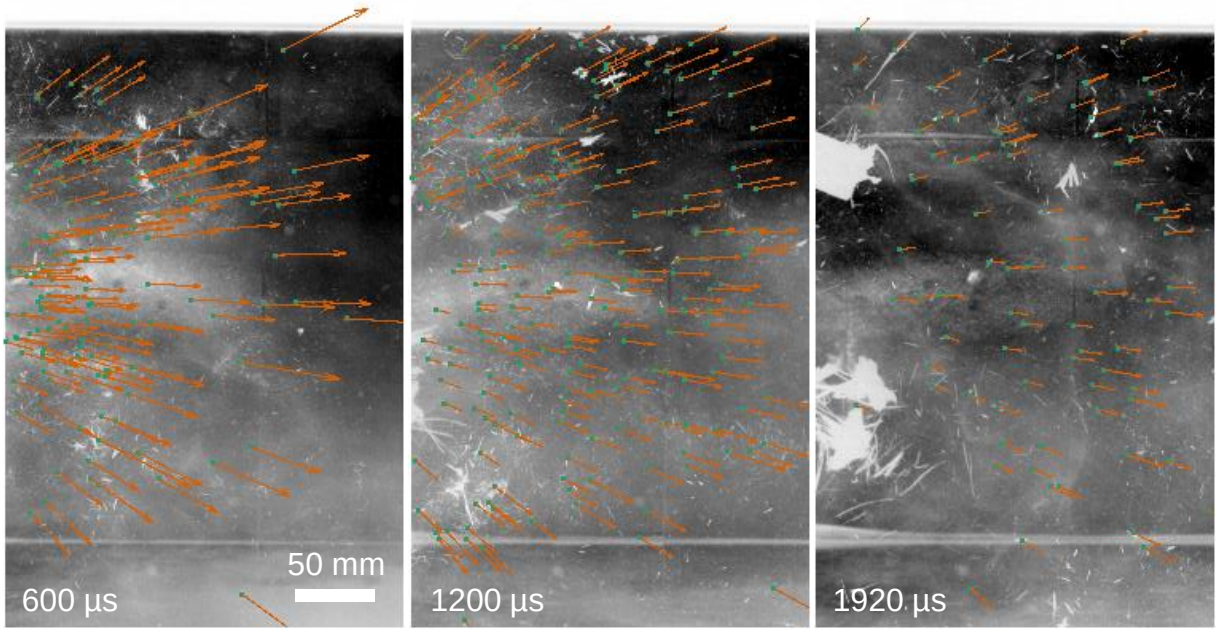

Figure 10. Fragments tracked in 2D in a single camera. Velocity vectors are scaled to the magnitude of the 2D fragment velocity.

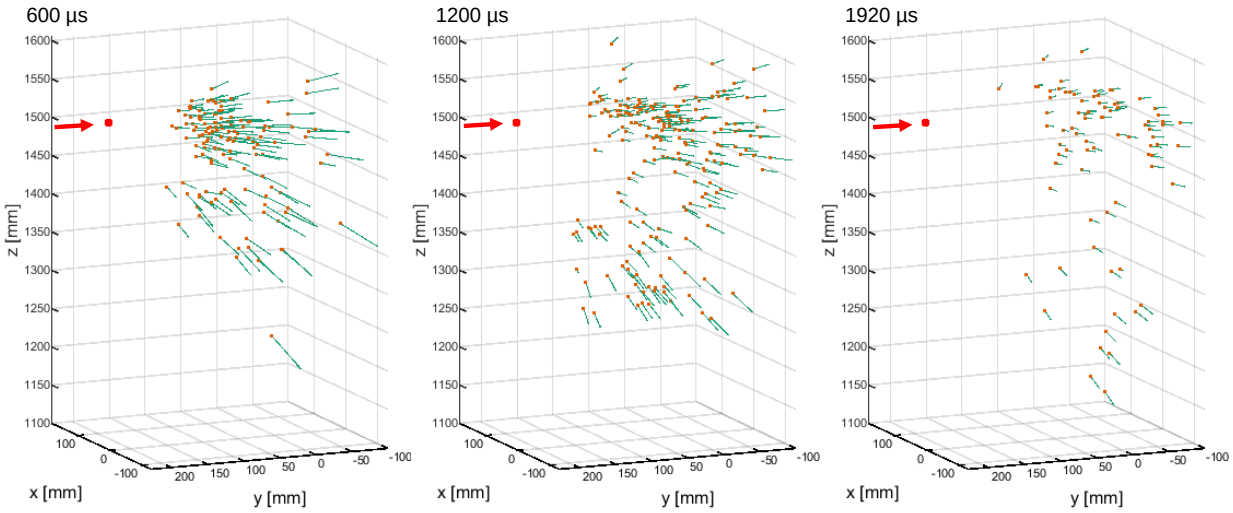

Figure 11. Fragments tracked in 3D. Velocity vectors are scaled to the magnitude of the 3D fragment velocity.

system has its origin at the centre of camera 1. This configuration of the CFRP panel angle leads to apparently symmetric fragmentation pattern when seen in 2D, such as in Fig. 10, but the clearly unsymmetrical reality is aparent when 3D data is available such as in Fig.11.

The data represented as points and vectors in Figs. 10 and 11 are also shown as histograms. Fig. 12 shows a histogram of fragment velocities. In this experiment, only the late-time, and hence slower fragments were tracked, ranging from 100 to 600 m/s. Being able to measure a fragment velocity distribution for a large and representative number of fragments in a single debris cloud represents one of the key achievements of our fragment tracking method as this type of data is rarely available from other experimental measurement methods.

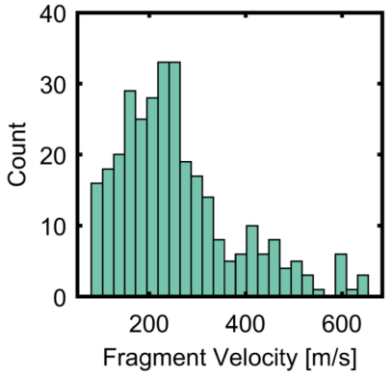

Figure 12. Fragment velocity distribution.

Fig. 13 shows the fragment size distribution of the debris cloud fragments. This histogram is plotted on a log scale because of the power law nature of the distribution.

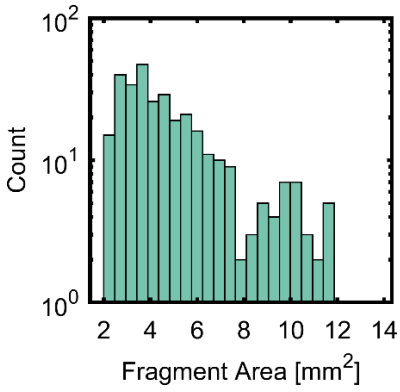

Figure 13. Fragment size distribution.

Fig. 14 combines the data shown in the velocity and size distributions to show a distribution of individual fragment kinetic energy. Fragment size data is converted into mass by using the thickness the CFRP ply layers, which constitute the vast majority of the tracked fragments based on post-mortem analysis. Fig. 14, also shown with a log scale, indicates a very strong representation of relatively low kinetic energy fragments.

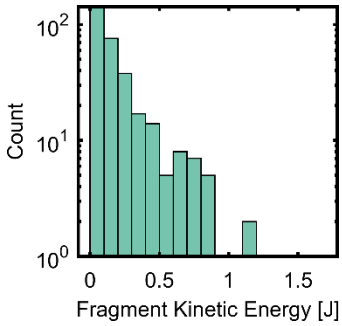

Figure 14. Fragment kinetic energy distribution.

As a final example of the types of data that can be

measured by the fragment tracking, we show the distribution of individual fragment momentum in Fig. 15. Fig. 15a shows a standard momentum histogram, while Fig. 15b presents the same data as a bivariate histogram covering fragment velocity and mass. The number of fragments in each bin is indicated by the colourbar. The grey iso-lines represent contours of constant momentum. Interestingly, Fig. 15b shows that the distributions of fragment momentum roughly follow the contours of constant momentum.

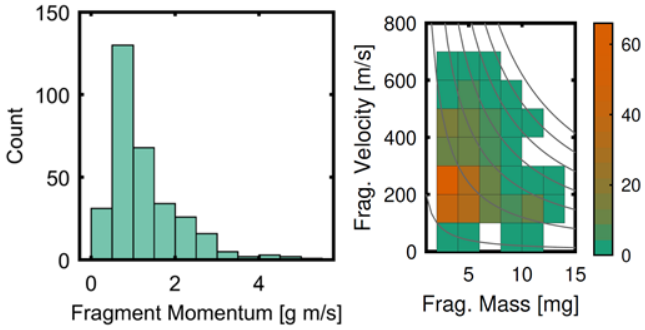

Figure 15. Fragment momentum distribution. Left: simple histogram. Right: bivariate histogram with colourbar indicating count and iso-lines indicating constant momentum.

5 APPLICATIONS

State-of-the-Art numerical models are usually calibrated to experiments via a qualitative comparison of the fragment cloud in terms of shape and expansion speed. Based on that fact, our fragment tracking method offers a novel way to increase the predictivity of numerical models since a quantitative match between experiments and numerical simulations can be achieved.

As an example of how the newly available fragment tracking data can be applied to validating numerical simulations, we present a FEM simulation of the same HVI on the CFRP panel and demonstrate a simple validation between the experiment and the simulation.

A detailed geometry of the sandwich structure, in which honeycomb cells are explicitly modelled is represented in Fig. 16. By using appropriate material models for the CFRP and aluminium components, and particularly an erosion-based failure model, in which elements are transformed to non-interacting mass points upon achievement of a critical strain, a realistic fragmentation pattern can be reproduced in the simulation. Fig. 18 shows a snap-shot of the numerical simulation, where the honeycomb core has been hidden from view to allow visualization of the fragmentation occurring between the CFRP face-sheets.

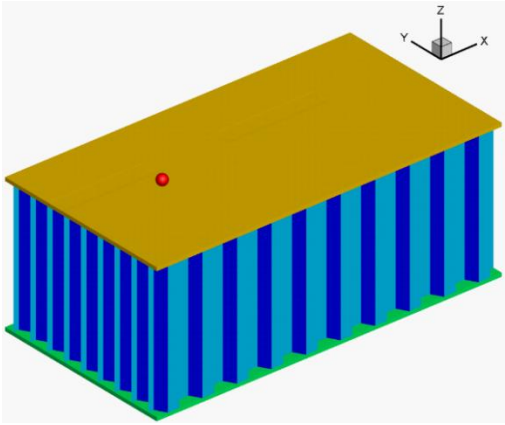

Figure 16. Numerical model of the CFRP honeycomb sandwich panel shown in Fig. 2.

A direct comparison between experiment and simulation must consider the particular limitations of each system. The experimental instrumentation exhibits some limitations, such as a surface projection-based evaluation of fragment volumes and minimum resolvable fragment size. Furthermore, only a subset of the fragments are tracked. Analysis of the size distribution of fragments tracked compared with collected post-impact fragment distributions indicate that the tracked fragments are a representative sample of the entire fragment cloud.

The numerical model introduces a bias in the fragment size distribution, which is strongly influenced by the mesh discretization. We assume that the artificial distribution of volumes does not introduce any bias in the distribution of velocities.

To overcome these limitations, we compare not an absolute fragment count, or even a normalized fragment mass, but work in percentage volume fraction. This allows a direct comparison between experiment and simulation. Fig. 17 shows such a comparison between the FEM simulation and the experiment regarding the fragment velocity distribution.

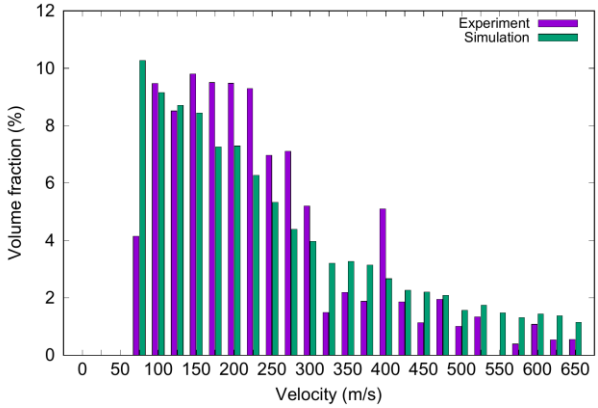

Figure 17. The fragment tracking data allows a direct and quantitative comparison between simulation and experiment.

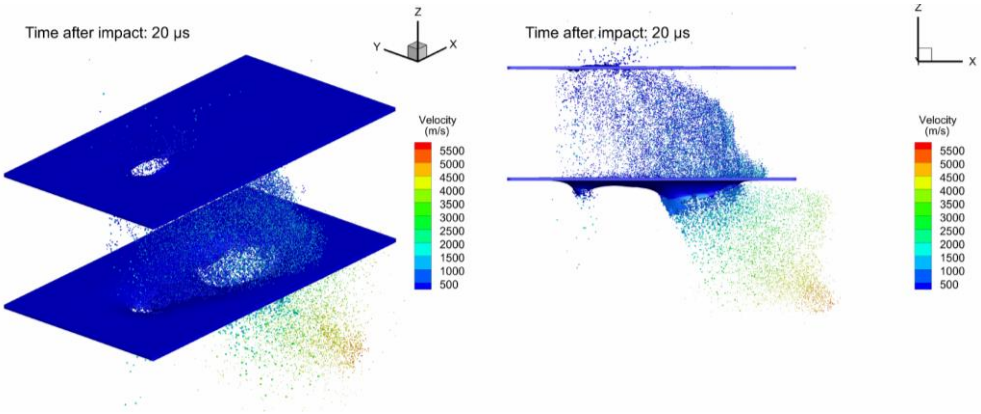

Figure 18. Simulated impact of the experiment shown in Fig. 3. Honeycomb core hidden.

Apart from some local discrepancies, both histograms show similar trends and are thus in good accordance. This result testifies to the quantitative validation of the numerical model by the experiment.

6 CONCLUSIONS

In this paper, we present the development of an advanced experimental measurement technique designed for measuring hypervelocity impact fragmentation in the laboratory. The measurement method focuses on the fragmentation caused by hypervelocity impacts, particularly on describing the properties of the fragments in the debris cloud that forms after impact. The setup uses two or more synchronized high-speed cameras to record image sequences of the in-flight debris fragments. The experimental images are processed with algorithms inspired from the fields of computer vision and photogrammetry. The main steps of the algorithm are: identifying fragments and their trajectories in each view, matching the fragments found in different views, and finally reconstructing the 3D locations and 3D trajectories of each fragment. The result is a method able to measure the 3D positions, velocities, and sizes of individual debris cloud fragments to a level of detail unmatched by other experimental methods. The paper focuses on the experimental method for measuring hypervelocity fragmentation, but fits within the wider context of validating numerical simulations of hypervelocity impact and satellite breakup. We present an outlook of how the experimental hypervelocity fragmentation data collected is being used to validate state-of-the-art numerical simulations to better predict the fragmentation patterns and satellite breakup effects.

7 ACKNOWLEDGEMENTS

The authors would like to acknowledge the excellent work of the laboratory personnel, especially of Benjamin Berger who operated the accelerator during the impact tests. Part of the work described herein was carried out under a program funded by, the BAAINBw under the project “Disruptive Fragmentierungsereignisse im Orbit und deren Konsequenzen”, Contract No. E/L2BB/IA089/EF107.

8 REFERENCES

[1] M. J. Cintala, L. Berthoud, and F. Hörz, “Ejection--velocity distributions from impacts into coarse--grained sand,” *Meteorit. {&} Planet. {...}*, vol. 34, no. June, pp. 605–623, 1999, doi: 10.1111/j.1945-5100.1999.tb01367.x.

[2] M. Raffel, C. E. Willert, S. T. Wereley, and J. Kompenhans, *Particle Image Velocimetry: A Practical Guide*. Springer Berlin Heidelberg, 2007.

[3] H. G. Maas, A. Gruen, and D. Papantoniou, “Particle tracking velocimetry in three-dimensional flows. Part 1.,” *Exp. Fluids*, vol. 15, no. 2, pp. 133–146, 1993, doi: 10.1007/BF00190953.

[4] J. T. Heineck, P. H. Schultz, and J. L. B. Anderson, “Application of Three-Component PIV to the Measurement of Hypervelocity Impact Ejecta,” *J. Vis.*, vol. 5, no. 3, pp. 233–241, 2002, doi: 10.1007/BF03182331.

[5] B. Hermalyn, J. T. Heineck, E. T. Schairer, and H. Peter, “Measurement of Ejecta from Hypervelocity Impacts with a Generalized High-Speed Two-Frame 3D Hybrid Particle Tracking Velocimetry Method,” 2014.

[6] M. Gulde, L. Kortmann, M. Ebert, E. Watson, J. Wilk, and F. Schäfer, “Robust optical tracking of individual ejecta particles in hypervelocity impact experiments,” *Meteorit. Planet. Sci.*, vol. 9, pp. 1–9, 2017, doi: 10.1111/maps.12958.

[7] M. Schimmerohn, E. Watson, M. Gulde, L. Kortmann, and F. Schaefer, “Measuring ejecta characteristics and momentum transfer in experimental simulation of kinetic impact,” *Acta Astronaut.*, no. March, 2018, doi: 10.1016/j.actaastro.2018.01.046.

[8] E. Watson, M. Gulde, L. Kortmann, M. Higashide, F. Schaefer, and S. Hiermaier, “Optical fragment tracking in hypervelocity impact experiments,” *Acta Astronaut.*, vol. 155, pp. 111–117, 2019, doi: 10.1016/j.actaastro.2018.11.036.

[9] E. Watson, H.-G. Maas, F. Schäfer, and S. Hiermaier, “Trajectory Based 3D Fragment Tracking in Hypervelocity Impact Experiments,” in *The International Archives of the Photogrammetry, Remote Sensing and Spatial Information Sciences*, 2018, vol. XLII, no. 2, doi: 10.5194/isprs-archives-XLII-2-1175-2018.

[10] E. Watson, N. Kunert, R. Putzar, H.-G. Maas, and S. Hiermaier, “Four-View Split-Image Fragment Tracking in Hypervelocity Impact Experiments,” *Int. J. Impact Eng.*, vol. 135, no. July 2019, p. 103405, 2019, doi: 10.1016/j.ijimpeng.2019.103405.

[11] Z. Zhang, “Flexible camera calibration by viewing a plane from unknown orientations,” *Proc. Seventh IEEE Int. Conf. Comput. Vis.*, no. c, pp. 666–673 vol.1, 1999, doi: 10.1109/ICCV.1999.791289.

[12] D. Brown, “Close-Range Camera Calibration,” in *Symposium on Close-Range Photogrammetry*, 1971, pp. 1–12.

[13] M. a Fischler and R. C. Bolles, “Random Sample Consensus: A Paradigm for Model Fitting with Applicatlons to Image Analysis and Automated Cartography,” in *Communications of the ACM*, 1981, vol. 24, pp. 381–395, doi: 10.1145/358669.358692.